Looped-Oxide Catalysis: A Solar Thermal Approach to Bio-Oil Deoxygenation (Supporting Information)

Cory Hargus, Ronald Michalsky [†], Andrew A. Peterson[*]

School of Engineering, Brown University, Providence, Rhode Island, 02912, United States.
[†] *Current address: Institute of Energy Technology, ETH Zurich, ML K 23 Sonneggstr. 3 CH-8092, Zurich, Switzerland.*
[*] *Corresponding author: Andrew_Peterson@brown.edu*

Appendix A: Derivation of solar absorption efficiency

The starting point for assessing the efficiency of any thermochemical cycle (TC) is the Carnot efficiency, which describes the maximum theoretical efficiency of a heat engine operating between a heat source at temperature T_{h} and a heat sink at temperature T_{c}. (For a simple derivation of the Carnot efficiency model as it is applied to solar TCs, see Ewan and Allen [1].)

$$\eta_{\mathrm{carnot}} = 1 - \frac{T_{\mathrm{c}}}{T_{\mathrm{h}}} \tag{1}$$

The Carnot efficiency model may be further refined for the case of a TC operated within a solar cavity, where some of the solar flux into the cavity of the furnace is lost to re-radiation, according to the Stefan-Boltzmann Law. Assuming perfect optics, perfect insulation and absorptivity and emissivity approaching unity, the absorption efficiency of a black body cavity is:

$$\eta_{\mathrm{absorption}} = \frac{IC - \sigma T_{\mathrm{h}}^4}{IC} \tag{2}$$

Here *C* denotes the "concentration ratio", which is a measure of the increase in solar flux intensity after amplification through the use of mirrors or condensing lenses. *I* represents the normal beam intensity of sunlight, taken to be 1 kW/m^2, and σ is the Stefan-Boltzmann constant. The maximum overall efficiency of a TC operated within a solar cavity is given by the product of the two efficiencies:

$$\eta_{\mathrm{overall}} = \eta_{\mathrm{carnot}} \times \eta_{\mathrm{absorption}} \tag{3}$$

Finally, by differentiating η_{overall} with respect to T_{h}, setting the resulting expression equal to zero and solving for *C*, we arrive at the analytical solution for the optimum concentration ratio corresponding to any given solar cavity temperature.

$$C_{\mathrm{optimum}} = \frac{\sigma T_{\mathrm{h}}^4 (4T_{\mathrm{h}} - 3T_{\mathrm{c}})}{I T_{\mathrm{c}}} \tag{4}$$

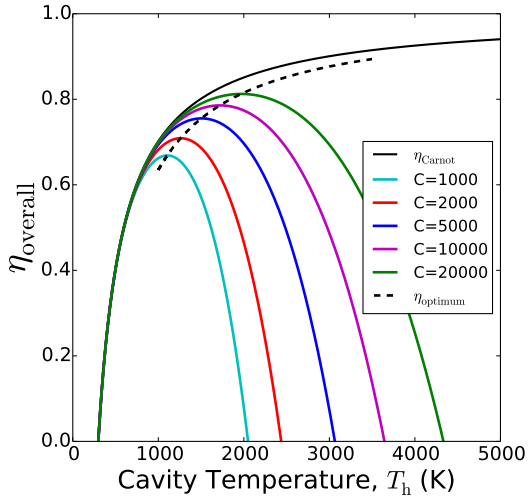

Figure 1: Overall efficiency of a solar furnace, η_{overall}, for select concentration ratios and optimum efficiency, η_{optimum}, as functions of temperature. Adapted from [2].

Figure 1 depicts the overall efficiency of a solar thermal metal oxide reduction process as a function of T_{h}, the cavity temperature. T_{c} has been set equal to 298 K and the overall efficiency is plotted along with the Carnot efficiency η_{optimum}, the efficiency of a solar cavity operating at the optimum concentration ratio, C_{optimum} for a given temperature. As the cavity temperature increases, η_{optimum} approaches the Carnot efficiency. The intersection of each efficiency curve with the x-axis is the stagnation temperature for a solar cavity operating at a given concentration ratio. This is the temperature at which the rate of absorption of solar thermal energy is in equilibrium with the rate of black-body re-radiation.

Appendix B: Exergy Analysis

To evaluate the theoretical performance of the five candidate looped-oxide catalysis (LOC) materials identified in Section 3, we have developed an exergy analysis for each material, with the goal of identifying areas of greatest loss and comparing between theoretical performances of the candidate oxide cycles. This analysis is modeled after the approach taken in [3]. Energy losses due to heat dissipation through the reactor walls and due to the circulation of an inert carrier gas and the operation of solids conveyors are neglected at this point. Consistent with the analysis presented in this perspective, the deoxygenation of acetic acid to acetaldehyde has been used as a model bio-oil deoxygenation reaction.

A flow diagram for the LOC process is presented in Figure 2. This schematic set up consists of a solar electrothermal furnace for the reduction of the metal oxide, a cooling device and an upgrading reactor in which acetic acid oxidizes the reduced metal oxide, reforming the higher-valence metal oxide and yielding the deoxygenated product, acetaldehyde. All steps are assumed to take place at 1 bar of total pressure.

The cycle begins with the solar heating of acetic acid to 500 K and the solar heating of the metal oxide to 1500 K, followed by dissociation of the metal oxide to the reduced oxide and oxygen gas. For many metal oxides, the limitations of current solar concentration optical systems and materials prohibit operation at the temperatures required for pure-thermal dissociation. Therefore,

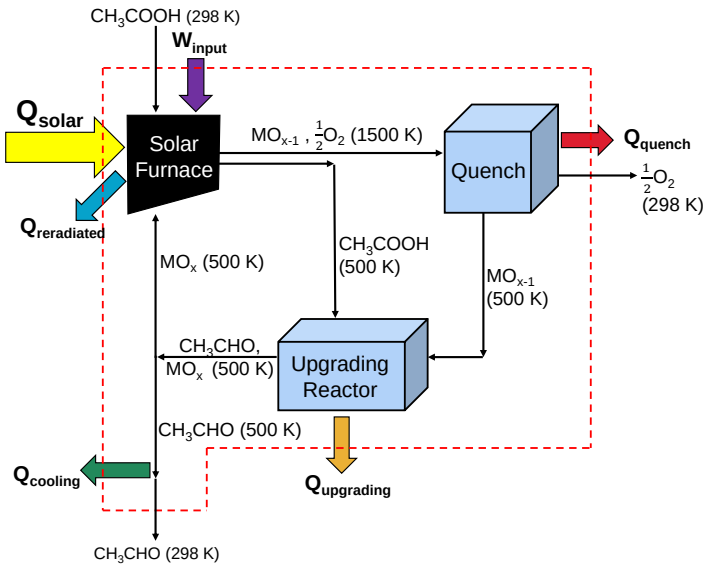

Figure 2: Flow diagram of the LOC upgrading of acetic acid to acetaldehyde used in the exergy analysis.

a solar furnace operating temperature of 1500 K is adopted in this analysis, where all additional work is added to the solar reactor via electrothermal reduction. The optimum concentration ratio corresponding to a cavity temperature of 1500 K is used: $C_{\text{optimum}} = 4920$. The three most common solar optical concentration setups, depicted in Figure 3, are parabolic trough, tower, and dish systems [4]. The parabolic trough concentrator, which can only achieve concentration ratios of 30 to 100, uses a linear parabolic optical reflector to concentrate sunlight onto a collector along the focal line of the trough. Although this concentration setup is generally incapable of reducing the metal oxides commonly used in water splitting and CO_2 splitting applications, it may find application in driving the reduction of weakly-bound metal oxides in LOC deoxygenation of alcohols, phenols, etc. In the tower arrangement, which exhibits typical concentration ratios of 500 to 1000, a field of dual-axis heliostats reflect sunlight onto a single focal point in a collecting tower. Finally, the dish collector can achieve concentration ratios of 1000-10000 and utilizes a parabolic dish reflector which tracks the sun along two axes, focusing sunlight onto a single receiving cavity at the focal point of the dish [5].

After reduction in the solar electrothermal furnace, the reduced oxide is cooled to 500 K while oxygen is vented from the cycle at 298 K. For the candidate oxides with gaseous or metastable reduction products (namely: Zn, Cd, FeO and SnO) this cooling step must involve rapid quenching to control particle nucleation size and phase stability. Therefore it is assumed in this analysis that no heat is recovered during quenching or cooling of products. In the next step, the reduced oxide is sent to the upgrading reactor where it is re-oxidized by acetic acid, rejecting additional heat from the cycle and yielding acetaldehyde, which exits the cycle at 298 K after additional cooling. By considering only the chemical inputs and outputs to the cycle enclosed in the dotted red line in Figure 2, it is easy to see that the net result of the cycle is the dissociation of acetic acid to form acetaldehyde and oxygen via the input of solar heat and electrolytic work.

$$\mathrm{CH_3COOH} \xrightarrow[\dot{W}_{\text{input}}]{\dot{Q}_{\text{solar}}} \mathrm{CH_3CHO} + \frac{1}{2}\mathrm{O_2} \tag{5}$$

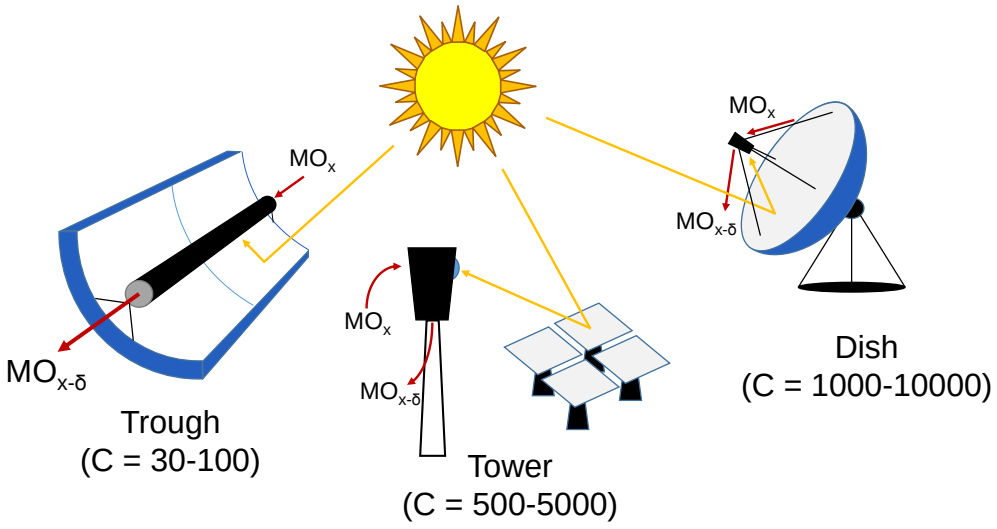

Figure 3: The three broad categories of solar collection schemes for the thermal reduction of metal oxides and typical ranges [4] of concentration ratios (C) achievable with each setup.

Therefore, the exergy efficiency of the process may be defined as:

$$\eta_{\text{exergy}} = \frac{\dot{n}_{\text{CH}_3\text{COOH}}\,\Delta\text{G}_{\text{rxn}}}{\dot{Q}_{\text{solar}} + \frac{\dot{W}_{\text{input}}}{\eta_{\text{PV}}}} \tag{6}$$

Here, $\dot{n}_{\text{CH}_3\text{COOH}}$ denotes the molar flow rate of acetic acid into the upgrading reactor, which is set equal to 1 mole/second and $\Delta\text{G}_{\text{rxn}}$ refers to the Gibbs free energy of the deoxygenation of one mole of acetic acid to acetaldehyde (Equation 5) at 298 K. $\dot{W}_{\text{input}}$ represents the additional work provided to the solar furnace to drive the metal oxide reduction reaction. For this analysis, we have assumed that this additional work is provided by an array of ideal p-n junction photovoltaic (PV) solar cells operating at the Shockley-Queisser limiting efficiency of $\eta_{\text{PV}} = 33.7\%$. $\dot{Q}_{\text{solar}}$ is the solar heat supplied to the reactor, and is given by the quotient of the total heat required by the solar reactor and the absorption efficiency (see Appendix A).

$$\dot{Q}_{\text{solar}} = \frac{1}{\eta_{\text{absorption}}}\Bigg[\dot{n}_{\text{MO}_\text{x}}\Delta\text{H}\,|_{\text{MO}_\text{x}(500\text{K})\rightarrow\text{MO}_{\text{x}-\delta}(1500\text{K})+\frac{\delta}{2}\text{O}_2(1500\text{K})} + \dot{n}_{\text{CH}_3\text{COOH}}\Delta\text{H}\,|_{\text{CH}_3\text{COOH}(298\text{K})\rightarrow\text{CH}_3\text{COOH}(500K)}\Bigg] \tag{7}$$

In the above equation, $\dot{n}_{\text{MO}_\text{x}}$ denotes the molar flow rate of metal oxide into the solar furnace, which is set equal to $\frac{1}{\delta}$ moles per second in order to balance the flow of acetic acid into the upgrading reactor. The exergy efficiencies of each of the candidate cycles are listed in Table 1. Also provided in Table 1 is the required heliostat and photovoltaic (PV) area of each cycle, assuming a solar tower collector as depicted in Figure 3. These quantities are defined as the solar collection areas required to gather sufficient solar thermal and electrical energy to drive each cycle at a rate of 1 mole of acetaldehyde produced per second.

Table 1: Efficiency analysis results for candidate LOC upgrading cycles.

Reaction Set	η_{exergy}	$\dot{W}_{\text{input}}$ (kW)	Heliostat Area (m^2)	PV Area (m^2)
$ZnO \rightarrow Zn + \frac{1}{2}O_2$ $CH_3COOH + Zn \rightarrow$ $CH_3CHO + ZnO$	27.5%	164	392	485
$CdO \rightarrow Cd + \frac{1}{2}O_2$ $CH_3COOH + Cd \rightarrow$ $CH_3CHO + CdO$	42.6%	62	382	185
$Fe_3O_4 \rightarrow 3\,FeO + \frac{1}{2}O_2$ $CH_3COOH + 3\,FeO \rightarrow$ $CH_3CHO + Fe_3O_4$	31.6%	420	764	344
$2\,CeO_2 \rightarrow Ce_2O_3 + \frac{1}{2}O_2$ $CH_3COOH + Ce_2O_3 \rightarrow$ $CH_3CHO + 2\,CeO_2$	25.8%	179	406	530
$SnO_2 \rightarrow SnO + \frac{1}{2}O_2$ $CH_3COOH + SnO \rightarrow$ $CH_3CHO + SnO_2$	26.9%	134	500	397

$$\text{Heliostat Area} = \frac{\dot{Q}_{\text{solar}}}{I} \tag{8}$$

$$\text{PV Area} = \frac{\dot{W}_{\text{input}}}{\eta_{\text{PV}} \times I} \tag{9}$$

We have also calculated the value of each heat loss term illustrated in Figure 2 for the five candidate cycles. Decomposing the heat transfer out of the TC into its constituent parts allows for a comparison of the relative contribution of each term. This is illustrated in Figure 4. Performing an energy balance on the cycle in Figure 2 (within the red dotted line) indicates that the solar heat, $\dot{Q}_{\text{solar}}$, balances with the sum of the heat loss terms plus the effective change in chemical enthalpy of the cycle in net, ΔH_{eff}, which is defined as the enthalpy of the net upgrading reaction at 298 K and 1 bar total pressure, minus the total electrical work added during the solar thermal reduction of the metal oxide.

$$\dot{Q}_{\text{solar}} = \dot{Q}_{\text{reradiated}} + \dot{Q}_{\text{quench}} + \dot{Q}_{\text{upgrading}} + \dot{Q}_{\text{cooling}} + \Delta H_{\text{eff}} \tag{10}$$

The net work accomplished by the cycle is indicated in Figure 4 by the distance between the dotted line and the top of each bar and is defined as follows:

$$\dot{W}_{\text{net}} = \dot{n}_{CH_3COOH} \Delta G_{\text{rxn}} - \dot{W}_{\text{input}} \tag{11}$$

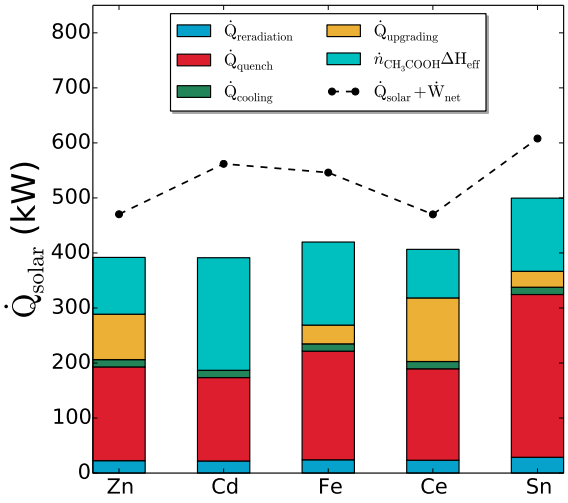

Figure 4: Heat loss terms in the exergy model for acetic acid selective deoxygenation to acetaldehyde, where the total height of each bar gives the total solar influx, $\dot{Q}_{\mathrm{solar}}$.

where ΔG_{rxn} again refers to the Gibbs free energy of the reaction at 298 K of one mole of acetic acid to acetaldehyde (Equation 5).

Due to the low solar furnace operation temperature of 1500 K, the re-radiation losses are relatively small, with most heat loss occurring during the quenching or cooling step. We have assumed here that no quenching heat is recovered; typical quenching parameters make any heat recovery difficult. Low-temperature heat lost during the upgrading reaction, the HDO reaction and product cooling constitutes a relatively small component of the total heat loss, and has also been assumed non-recoverable. In practice, a small amount of pumping work will be required due to pressure drops occurring between various stages of the cycle.

Appendix C: Thermochemical quantities

Table 2: Reaction stoichiometry and thermochemical values used in construction of Figure 2 of the main text. The metal-oxygen bond strength is defined as the ΔH of the reduction reaction, which is always normalized to the formation of $\frac{1}{2}$ moles of O_2. The Gibbs free energy of the metal oxide reduction and acetic acid deoxygenative upgrading reaction reactions are also provided in the columns labeled ΔG_r and ΔG_u, respectively. The final column lists the molecular weight ratio of the zero-valent metal or low-valence metal oxide to acetic acid in each reaction. This value is represented graphically in Figure 2 of the main text as the inverse of the weighting (size) of each point.

Metal Oxide Reduction	Bio-oil Upgrading	M-O Bond Strength (kJ/mol)	ΔG_r (kJ/mol)	ΔG_u (kJ/mol)	Metal/Acid wt. Ratio
$3Fe_2O_3 \rightarrow 2Fe_3O_4 + \frac{1}{2}O_2$	$2Fe_3O_4 + CH_3COOH \rightarrow 3Fe_2O_3 + CH_3CHO$	235.978	33.03686	51.50783	7.711365
$Fe_3O_4 \rightarrow 3FeO + \frac{1}{2}O_2$	$3FeO + CH_3COOH \rightarrow Fe_3O_4 + CH_3CHO$	302.251	111.9764	-12.9453	3.589227
$FeO \rightarrow Fe + \frac{1}{2}O_2$	$Fe + CH_3COOH \rightarrow FeO + CH_3CHO$	272.044	175.0502	-18.4222	0.929987
$\frac{1}{4}Fe_3O_4 \rightarrow \frac{3}{4}Fe + \frac{1}{2}O_2$	$\frac{3}{4}Fe + CH_3COOH \rightarrow \frac{1}{4}Fe_3O_4 + CH_3CHO$	279.5958	159.2817	-17.0529	0.69749
$Fe_2O_3 \rightarrow 2FeO + \frac{1}{2}O_2$	$2FeO + CH_3COOH \rightarrow Fe_2O_3 + CH_3CHO$	280.16	85.66321	6.77808	2.392818
$Mn_3O_4 \rightarrow 3MnO + \frac{1}{2}O_2$	$3MnO + CH_3COOH \rightarrow Mn_3O_4 + CH_3CHO$	232.136	43.97802	51.98201	3.543816
$MnO \rightarrow Mn + \frac{1}{2}O_2$	$Mn + CH_3COOH \rightarrow MnO + CH_3CHO$	385.221	274.3574	-128.072	0.91485
$\frac{1}{3}Cr_2O_3 \rightarrow \frac{2}{3}Cr + \frac{1}{2}O_2$	$\frac{2}{3}Cr + CH_3COOH \rightarrow \frac{1}{3}Cr_2O_3 + CH_3CHO$	379.9003	246.0345	-111.499	0.577239
$Al_2O_3 \rightarrow 2AlO + \frac{1}{2}O_2$	$2AlO + CH_3COOH \rightarrow Al_2O_3 + CH_3CHO$	1812.928	1153.696	-1391.26	1.431474
$2AlO \rightarrow Al_2O + \frac{1}{2}O_2$	$Al_2O + CH_3COOH \rightarrow 2AlO + CH_3CHO$	-267.777	-199.635	494.4735	1.165036
$Al_2O \rightarrow 2Al + \frac{1}{2}O_2$	$2Al + CH_3COOH \rightarrow Al_2O + CH_3CHO$	130.541	244.9732	39.18734	0.898631
$\frac{1}{3}Al_2O_3 \rightarrow \frac{2}{3}Al + \frac{1}{2}O_2$	$\frac{2}{3}Al + CH_3COOH \rightarrow \frac{1}{3}Al_2O_3 + CH_3CHO$	558.564	399.678	-285.866	0.299544
$MgO \rightarrow Mg + \frac{1}{2}O_2$	$Mg + CH_3COOH \rightarrow MgO + CH_3CHO$	601.241	424.4333	-327.406	0.404737
$CaO \rightarrow Ca + \frac{1}{2}O_2$	$Ca + CH_3COOH \rightarrow CaO + CH_3CHO$	635.089	478.3692	-362.569	0.667395
$SrO \rightarrow Sr + \frac{1}{2}O_2$	$Sr + CH_3COOH \rightarrow SrO + CH_3CHO$	592.036	443.2446	-322.398	1.459084
$BaO \rightarrow Ba + \frac{1}{2}O_2$	$Ba + CH_3COOH \rightarrow BaO + CH_3CHO$	553.543	397.4632	-284.152	2.286826
$ZnO \rightarrow Zn + \frac{1}{2}O_2$	$Zn + CH_3COOH \rightarrow ZnO + CH_3CHO$	350.46	162.8706	-78.2073	1.088901
$CdO \rightarrow Cd + \frac{1}{2}O_2$	$Cd + CH_3COOH \rightarrow CdO + CH_3CHO$	258.99	64.79342	9.619015	1.871914
$3TiO_2(R) \rightarrow Ti_3O_5 + \frac{1}{2}O_2$	$Ti_3O_5 + CH_3COOH \rightarrow 3TiO_2(R) + CH_3CHO$	375.095	213.7271	-112.972	3.724095
$2Ti_3O_5 \rightarrow 3Ti_2O_3 + \frac{1}{2}O_2$	$3Ti_2O_3 + CH_3COOH \rightarrow 2Ti_3O_5 + CH_3CHO$	355.64	255.3872	-98.1734	7.181752
$Ti_2O_3 \rightarrow 2TiO + \frac{1}{2}O_2$	$2TiO + CH_3COOH \rightarrow Ti_2O_3 + CH_3CHO$	435.554	310.6243	-199.619	2.127479
$TiO \rightarrow Ti + \frac{1}{2}O_2$	$Ti + CH_3COOH \rightarrow TiO + CH_3CHO$	542.665	403.0029	-258.969	0.797317
$\frac{1}{3}Ti_2O_3 \rightarrow \frac{2}{3}Ti + \frac{1}{2}O_2$	$\frac{2}{3}Ti + CH_3COOH \rightarrow \frac{1}{3}Ti_2O_3 + CH_3CHO$	506.9613	372.21	-239.185	0.531545
$\frac{1}{5}Ti_3O_5 \rightarrow \frac{3}{5}Ti + \frac{1}{2}O_2$	$\frac{3}{5}Ti + CH_3COOH \rightarrow \frac{1}{5}Ti_3O_5 + CH_3CHO$	491.8292	360.5277	-225.084	0.47839
$\frac{1}{2}TiO_2(R) \rightarrow \frac{1}{2}Ti + \frac{1}{2}O_2$	$\frac{1}{2}Ti + CH_3COOH \rightarrow \frac{1}{2}TiO_2(R) + CH_3CHO$	472.3735	336.061	-206.399	0.398659
$\frac{1}{2}Ti_3O_5 \rightarrow 3/2TiO + \frac{1}{2}O_2$	$3/2TiO + CH_3COOH \rightarrow \frac{1}{2}Ti_3O_5 + CH_3CHO$	415.5755	296.815	-174.257	1.595609
$TiO_2(R) \rightarrow TiO + \frac{1}{2}O_2$	$TiO + CH_3COOH \rightarrow TiO_2(R) + CH_3CHO$	402.082	269.119	-153.829	1.063739
$2TiO_2(R) \rightarrow Ti_2O_3 + \frac{1}{2}O_2$	$Ti_2O_3 + CH_3COOH \rightarrow 2TiO_2(R) + CH_3CHO$	368.61	227.6138	-108.039	2.393917
$ZrO_2 \rightarrow ZrO + \frac{1}{2}O_2$	$ZrO + CH_3COOH \rightarrow ZrO_2 + CH_3CHO$	1156.039	757.5717	-797.391	1.785521
$ZrO \rightarrow Zr + \frac{1}{2}O_2$	$Zr + CH_3COOH \rightarrow ZrO + CH_3CHO$	-58.576	16.15024	237.2453	1.519099
$\frac{1}{2}ZrO_2 \rightarrow \frac{1}{2}Zr + \frac{1}{2}O_2$	$\frac{1}{2}Zr + CH_3COOH \rightarrow \frac{1}{2}ZrO_2 + CH_3CHO$	548.7315	386.861	-280.073	0.75955
$\frac{1}{2}HfO_2 \rightarrow \frac{1}{2}Hf + \frac{1}{2}O_2$	$\frac{1}{2}Hf + CH_3COOH \rightarrow \frac{1}{2}HfO_2 + CH_3CHO$	572.371	421.6384	-289.721	1.486144
$CoO \rightarrow Co + \frac{1}{2}O_2$	$Co + CH_3COOH \rightarrow CoO + CH_3CHO$	237.944	129.0262	19.95768	0.981377
$2RhO_2 \rightarrow Rh_2O_3 + \frac{1}{2}O_2$	$Rh_2O_3 + CH_3COOH \rightarrow 2RhO_2 + CH_3CHO$	12.36	478.9023	46.19554	4.226532
$NiO \rightarrow Ni + \frac{1}{2}O_2$	$Ni + CH_3COOH \rightarrow NiO + CH_3CHO$	239.701	107.9597	25.9408	0.97733
$MoO_3 \rightarrow MoO_2 + \frac{1}{2}O_2$	$MoO_2 + CH_3COOH \rightarrow MoO_3 + CH_3CHO$	156.147	73.12376	99.49551	2.130493
$\frac{1}{2}MoO_2 \rightarrow \frac{1}{2}Mo + \frac{1}{2}O_2$	$\frac{1}{2}Mo + CH_3COOH \rightarrow \frac{1}{2}MoO_2 + CH_3CHO$	294.47	163.1467	-28.4742	0.798816
$GeO_2 \rightarrow GeO + \frac{1}{2}O_2$	$GeO + CH_3COOH \rightarrow GeO_2 + CH_3CHO$	533.711	132.842	-186.732	1.475553
$GeO \rightarrow Ge + \frac{1}{2}O_2$	$Ge + CH_3COOH \rightarrow GeO + CH_3CHO$	46.191	149.1889	144.3271	1.209132
$\frac{1}{2}GeO_2 \rightarrow \frac{1}{2}Ge + \frac{1}{2}O_2$	$\frac{1}{2}Ge + CH_3COOH \rightarrow \frac{1}{2}GeO_2 + CH_3CHO$	289.951	141.2166	-21.2024	0.604566
$SnO_2 \rightarrow SnO + \frac{1}{2}O_2$	$SnO + CH_3COOH \rightarrow SnO_2 + CH_3CHO$	295.053	142.3815	-21.8907	2.24323
$SnO \rightarrow Sn + \frac{1}{2}O_2$	$Sn + CH_3COOH \rightarrow SnO + CH_3CHO$	285.77	130.2814	-17.372	1.976808
$\frac{1}{2}SnO_2 \rightarrow \frac{1}{2}Sn + \frac{1}{2}O_2$	$\frac{1}{2}Sn + CH_3COOH \rightarrow \frac{1}{2}SnO_2 + CH_3CHO$	290.4115	137.9402	-19.6313	0.988404
$PbO \rightarrow Pb + \frac{1}{2}O_2$	$Pb + CH_3COOH \rightarrow PbO + CH_3CHO$	218.062	77.45839	51.18705	3.450379
$Nb_2O_5 \rightarrow 2NbO_2 + \frac{1}{2}O_2$	$2NbO_2 + CH_3COOH \rightarrow Nb_2O_5 + CH_3CHO$	309.616	194.3468	-53.1201	4.159939
$NbO_2 \rightarrow NbO + \frac{1}{2}O_2$	$NbO + CH_3COOH \rightarrow NbO_2 + CH_3CHO$	375.305	251.4668	-118.721	1.813547
$NbO \rightarrow Nb + \frac{1}{2}O_2$	$Nb + CH_3COOH \rightarrow NbO + CH_3CHO$	419.655	281.1146	-144.854	1.547109
$\frac{1}{2}NbO_2 \rightarrow \frac{1}{2}Nb + \frac{1}{2}O_2$	$\frac{1}{2}Nb + CH_3COOH \rightarrow \frac{1}{2}NbO_2 + CH_3CHO$	397.48	266.2907	-131.788	0.773554
$\frac{1}{5}Nb_2O_5 \rightarrow 2/5Nb + \frac{1}{2}O_2$	$2/5\ Nb + CH_3COOH \rightarrow \frac{1}{5}Nb_2O_5 + CH_3CHO$	379.9072	251.9019	-116.054	0.618844
$\frac{1}{3}Nb_2O_5 \rightarrow \frac{2}{3}NbO + \frac{1}{2}O_2$	$\frac{2}{3}NbO + CH_3COOH \rightarrow \frac{1}{3}Nb_2O_5 + CH_3CHO$	353.4087	232.4268	-96.854	1.209032
$Ta_2O_5 \rightarrow 2TaO_2 + \frac{1}{2}O_2$	$2TaO_2 + CH_3COOH \rightarrow Ta_2O_5 + CH_3CHO$	1644.312	975.7338	-1195.85	7.092162
$TaO_2 \rightarrow TaO + \frac{1}{2}O_2$	$TaO + CH_3COOH \rightarrow TaO_2 + CH_3CHO$	393.296	287.2902	-150.18	3.279642
$TaO \rightarrow Ta + \frac{1}{2}O_2$	$Ta + CH_3COOH \rightarrow TaO + CH_3CHO$	-192.464	-74.4166	387.0032	3.01322
$\frac{1}{5}Ta_2O_5 \rightarrow 2/5Ta + \frac{1}{2}O_2$	$2/5Ta + CH_3COOH \rightarrow \frac{1}{5}Ta_2O_5 + CH_3CHO$	409.1952	280.2962	-144.442	1.205288
$\frac{1}{3}Ta_2O_5 \rightarrow \frac{2}{3}TaO + \frac{1}{2}O_2$	$\frac{2}{3}TaO + CH_3COOH \rightarrow \frac{1}{3}Ta_2O_5 + CH_3CHO$	810.3013	516.7714	-498.738	2.186428

Oxide Reduction	Bio-oil Upgrading	M-O Bond Strength (kJ/mol)	ΔG_{red} (kJ/mol)	ΔG_{upg} (kJ/mol)	Metal/Acid wt. Ratio
$Li_2O \rightarrow 2Li + \frac{1}{2}O_2$	$2Li + CH_3COOH \rightarrow Li_2O + CH_3CHO$	598.73	399.7812	-316.603	0.231169
$\frac{1}{3}B_2O_3 \rightarrow \frac{2}{3}B + \frac{1}{2}O_2$	$\frac{2}{3}B + CH_3COOH \rightarrow \frac{1}{3}B_2O_3 + CH_3CHO$	423.9787	303.1768	-160.285	0.120019
$2CeO_2 \rightarrow Ce_2O_3 + \frac{1}{2}O_2$	$Ce_2O_3 + CH_3COOH \rightarrow 2CeO_2 + CH_3CHO$	381.163	78.78053	-71.0108	5.465787
$\frac{1}{3}Ce_2O_3 \rightarrow \frac{2}{3}Ce + \frac{1}{2}O_2$	$\frac{2}{3}Ce + CH_3COOH \rightarrow \frac{1}{3}Ce_2O_3 + CH_3CHO$	598.7303	703.414	-340.173	1.555502
$\frac{1}{2}CeO_2 \rightarrow \frac{1}{2}Ce + \frac{1}{2}O_2$	$\frac{1}{2}Ce + CH_3COOH \rightarrow \frac{1}{2}CeO_2 + CH_3CHO$	544.3385	390.1538	-272.883	1.166626
$\frac{1}{3}Ga_2O_3 \rightarrow \frac{2}{3}Ga + \frac{1}{2}O_2$	$\frac{2}{3}Ga + CH_3COOH \rightarrow \frac{1}{3}Ga_2O_3 + CH_3CHO$	363.0317	200.0468	-90.1847	0.774037
$BeO \rightarrow Be + \frac{1}{2}O_2$	$Be + CH_3COOH \rightarrow BeO + CH_3CHO$	608.354	452.7674	-329.833	0.150072
$\frac{1}{3}Y_2O_3 \rightarrow \frac{2}{3}Y + \frac{1}{2}O_2$	$\frac{2}{3}Y + CH_3COOH \rightarrow \frac{1}{3}Y_2O_3 + CH_3CHO$	635.1033	491.878	-366.04	0.986999
$\frac{1}{3}In_2O_3 \rightarrow \frac{2}{3}In + \frac{1}{2}O_2$	$\frac{2}{3}In + CH_3COOH \rightarrow \frac{1}{3}In_2O_3 + CH_3CHO$	308.5963	150.5445	-36.1553	1.274687
$\frac{1}{3}Sc_2O_3 \rightarrow \frac{2}{3}Sc + \frac{1}{2}O_2$	$\frac{2}{3}Sc + CH_3COOH \rightarrow \frac{1}{3}Sc_2O_3 + CH_3CHO$	636.2733	488.7037	-365.873	0.499084
$ThO_2 \rightarrow ThO + \frac{1}{2}O_2$	$ThO + CH_3COOH \rightarrow ThO_2 + CH_3CHO$	1201.31	807.9806	-840.997	4.130431
$ThO \rightarrow Th + \frac{1}{2}O_2$	$Th + CH_3COOH \rightarrow ThO + CH_3CHO$	25.104	139.4778	149.8541	3.863992
$\frac{1}{2}ThO_2 \rightarrow \frac{1}{2}Th + \frac{1}{2}O_2$	$\frac{1}{2}Th + CH_3COOH \rightarrow \frac{1}{2}ThO_2 + CH_3CHO$	613.207	473.7292	-345.571	1.931996
$\frac{1}{2}UO_2 \rightarrow \frac{1}{2}U + \frac{1}{2}O_2$	$\frac{1}{2}U + CH_3COOH \rightarrow \frac{1}{2}UO_2 + CH_3CHO$	542.4495	414.0214	-278.654	1.981878
$Cu_2O \rightarrow 2Cu + \frac{1}{2}O_2$	$2Cu + CH_3COOH \rightarrow Cu_2O + CH_3CHO$	170.707	59.96508	87.22384	2.116388
$\frac{1}{2}PtO_2 \rightarrow \frac{1}{2}Pt + \frac{1}{2}O_2$	$\frac{1}{2}Pt + CH_3COOH \rightarrow \frac{1}{2}PtO_2 + CH_3CHO$	-85.3535	-82.0273	301.9969	1.624276
$\frac{1}{2}ReO_2 \rightarrow \frac{1}{2}Re + \frac{1}{2}O_2$	$\frac{1}{2}Re + CH_3COOH \rightarrow \frac{1}{2}ReO_2 + CH_3CHO$	224.4715	174.1381	47.94445	1.550398
$RuO_4 \rightarrow RuO_3 + \frac{1}{2}O_2$	$RuO_3 + CH_3COOH \rightarrow RuO_4 + CH_3CHO$	105.855	-20.2631	157.6866	2.482341
$\frac{1}{2}RuO_2 \rightarrow \frac{1}{2}Ru + \frac{1}{2}O_2$	$\frac{1}{2}Ru + CH_3COOH \rightarrow \frac{1}{2}RuO_2 + CH_3CHO$	152.507	56.73922	110.4409	0.84153
$\frac{1}{2}OsO_4 \rightarrow \frac{1}{2}OsO_2 + \frac{1}{2}O_2$	$\frac{1}{2}OsO_2 + CH_3COOH \rightarrow \frac{1}{2}OsO_4 + CH_3CHO$	21.1145	89.80119	190.0686	1.850074
$\frac{1}{2}OsO_2 \rightarrow \frac{1}{2}Os + \frac{1}{2}O_2$	$\frac{1}{2}Os + CH_3COOH \rightarrow \frac{1}{2}OsO_2 + CH_3CHO$	147.486	29.35076	118.6875	1.583644
$SiO_2 \rightarrow SiO + \frac{1}{2}O_2$	$SiO + CH_3COOH \rightarrow SiO_2 + CH_3CHO$	810.441	416.3205	-454.742	0.734122
$SiO \rightarrow Si + \frac{1}{2}O_2$	$Si + CH_3COOH \rightarrow SiO + CH_3CHO$	100.416	227.6054	74.59653	0.467683
$\frac{1}{2}SiO_2 \rightarrow \frac{1}{2}Si + \frac{1}{2}O_2$	$\frac{1}{2}Si + CH_3COOH \rightarrow \frac{1}{2}SiO_2 + CH_3CHO$	455.4285	321.963	-190.073	0.233841
$\frac{1}{3}Sb_2O_3 \rightarrow \frac{2}{3}Sb + \frac{1}{2}O_2$	$\frac{2}{3}Sb + CH_3COOH \rightarrow \frac{1}{3}Sb_2O_3 + CH_3CHO$	240.1017	121.0933	25.19465	1.351621
$\frac{1}{3}Bi_2O_3 \rightarrow \frac{2}{3}Bi + \frac{1}{2}O_2$	$\frac{2}{3}Bi + CH_3COOH \rightarrow \frac{1}{3}Bi_2O_3 + CH_3CHO$	191.294	68.38608	74.07074	2.320014

Appendix D: Experimental yields

In addition to the values for selectivity to organic products presented in Section 4.2 of the main text, we present herein the yield of each product, as measured in the experimental setup described in Section 4.1 of the main text. Figures 5 and 6 below give the carbon-weighted yields of each reaction product in the ZnO HDO and Zn LOC experiments, as well as the total yield summed over all products. The carbon-weighted yield is defined as:

$$\text{Yield}_i(\%) = \frac{p_i C_i}{2p_{\text{AcOH}}} \tag{12}$$

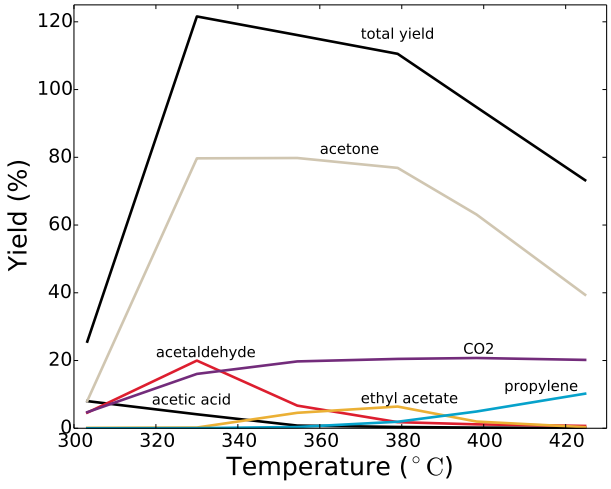

Figure 5: Carbon-weighted yield (see Equation 12) of all products of ZnO-catalyzed HDO plotted as a function of temperature.

As in Equation 7, p_i and C_i denote the partial pressure and number of carbon atoms in product i,

respectively. p_{AcOH} denotes the partial pressure of acetic acid in the feed stream to the upgrading reactor and the number 2 in the denominator derives from the number of carbon atoms in acetic acid. Notably, the total yield in Figure 5 is not consistently 100%, indicating that a carbon-balance on the reactor is not closed. This could be explained by the carbon deposition and subsequent decomposition and desorption at the metal oxide surface. Figure 6 illustrates that the carbon-balance is closed for the LOC deoxygenation of acetic acid to acetaldehyde at 350°C, as the total yield remains close to 100% and stabilizes after the reaction has proceeded for 100 minutes.

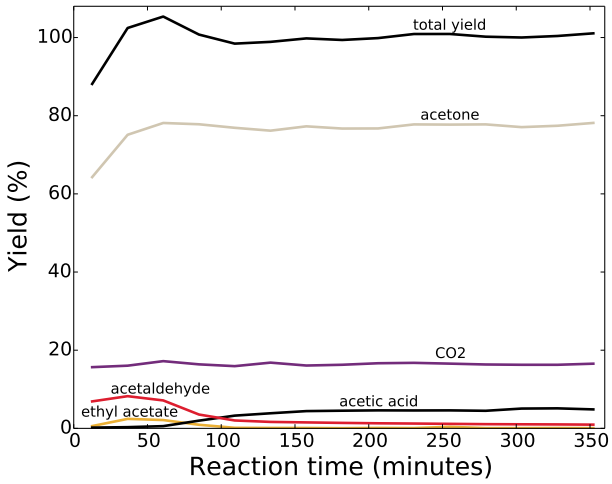

Figure 6: Carbon-weighted yield of all LOC products plotted as a function of reaction time.

References

[1] Ewan, B.; Allen, R. Limiting thermodynamic efficiencies of thermochemical cycles used for hydrogen generation. *Green Chem.* **2006**; , 988–994.

[2] Fletcher, E.a.; Moen, R.L. Hydrogen and oxygen from water. *Science* **1977**; 197, 1050–6.

[3] Steinfeld, A. Solar hydrogen production via a two-step water-splitting thermochemical cycle based on Zn/ZnO redox reactions. *Int. J. Hydrogen Energy* **2002**; 27, 611–619.

[4] Steinfeld, A.; Palumbo, R. Solar thermochemical process technology. *Encycl. Phys. Sci. Technol.* **2001**; 15, 237–256.

[5] Kodama, T.; Gokon, N. Thermochemical cycles for high-temperature solar hydrogen production. *Chem. Rev.* **2007**; 107, 4048–77.